Biomaterials Science

ROYAL SOCIETY OF CHEMISTRY

PAPER

View Article Online
View Journal | View Issue

Cite this: *Biomater. Sci.*, 2026, **14**, 2039

A thermosensitive hydrogel achieves sustained co-delivery of two therapeutic agents with distinct properties for preventing aseptic loosening

Yang Wang,[a] Xin Wang,[a] Hongjie Zhang,[a] Yaoben Wang,[a] Hancheng Wang,[a] Zhiyong Chen,[a] Jiandong Ding,[a] Xiaochun Peng*[b] and Lin Yu *[a,c]

Wear particle-induced prosthesis aseptic loosening severely affects the longevity of total joint arthroplasty. This condition arises from periprosthetic osteolysis, which is driven by excessive inflammation and enhanced bone resorption under particle stimulation. Herein, we develop an injectable hydrogel-based system co-encapsulating anti-inflammatory emodin (Emo) and anti-osteoporotic salmon calcitonin (sCT) to synergistically inhibit wear particle-induced aseptic loosening. This hydrogel is formulated from thermosensitive poly(lactic acid-*co*-glycolic acid)-*b*-poly(ethylene glycol)-*b*-poly(lactic acid-*co*-glycolic acid) triblock copolymers and water. The aqueous system undergoes a sol-to-gel phase transition upon heating with the transition temperature between room temperature and body temperature. Highly hydrophobic Emo is efficiently solubilized into micelles formed by the amphiphilic carrier polymers, while hydrophilic sCT is encapsulated within bovine serum albumin (BSA)-derived nanoparticles to suppress its initial burst release and prolong its release duration from the hydrogel matrix. This dual-delivery platform achieves simultaneous and continuous liberation of both therapeutic agents with distinct properties. In a mouse bone-implanted air pouch model, a single administration of the hydrogel formulation plus the sustained release of active Emo and sCT efficiently suppresses titanium particle-induced aseptic inflammation and osteolysis. Therefore, this local and long-acting co-delivery system holds great promise for preventing wear particle-induced aseptic loosening.

Received 22nd January 2026,
Accepted 11th February 2026

DOI: 10.1039/d6bm00096g

rsc.li/biomaterials-science

1. Introduction

Joints, especially synovial joints, play a critical role in ensuring the mobility and flexibility of the human body. Due to aging, injury, or diseases, individuals may experience significant joint pain, swelling and even stiffness, which can seriously impair their quality of life.[1–3] Fortunately, total joint arthroplasty (TJA) can restore the joint function of patients with end-stage joint diseases, thanks to advances in modern medicine and biomaterial science.[4,5] Nevertheless, TJA does not provide a permanent solution as expected, primarily due to prosthesis failure. Among all causes of prosthesis failure, aseptic loosening is the predominant factor, accounting for more than 30% of all cases.[5–8] This process initiates with implant wear debris generation, progresses through excessive inflammation, and ultimately results in enhanced bone resorption around the implant.[9,10] Early-stage complications like infection or mechanical instability can be addressed by improvements in surgical techniques and prothesis design optimization.[11,12] In contrast, aseptic loosening is a long-term process for which no effective preventive measures have been established so far.[13] The occurrence of TJA failure and subsequent revision impose substantial physical and financial burdens on patients, especially young individuals with high-activity levels.[5,7,12] Therefore, developing a straightforward and effective strategy to avert aseptic loosening is of critical importance and clinical value.

The general mechanism of aseptic loosening has been elucidated through decades of research. Wear particles, generated *via* repeated movements of the bearing surface of artificial joint over a long period of time,[13,14] induce innate immune responses in the tissues surrounding the prosthesis, especially triggering the phagocytosis of macrophages.[11,13] Upon activation, macrophages undergo phenotypic polarization and release various pro-inflammatory cytokines, thereby amplifying the chronic inflammatory responses and modulating the activity of surrounding cells, such as osteoclasts, osteoblasts

[a]*State Key Laboratory of Molecular Engineering of Polymers, Department of Macromolecular Science, Shanghai Stomatological Hospital and School of Stomatology, Fudan University, Shanghai 200438, P. R. China.*
E-mail: yu_lin@fudan.edu.cn
[b]*Department of Orthopedics, Shanghai Sixth People's Hospital Affiliated to Shanghai Jiao Tong University School of Medicine, Shanghai 200233, P. R. China.*
E-mail: dr.xcpeng@shsmu.edu.cn
[c]*Shanghai Key Laboratory of Gene Editing and Cell Therapy for Rare Diseases, Fudan University, Shanghai 200031, P. R. China*

and fibroblasts.[9,10,12] Over-activation of osteoclasts and their precursors, coupled with damage to osteoblasts and mesenchymal stem cells (MSCs), disrupts bone homeostasis, leading to osteolysis and, macroscopically, implant loosening.[11,15–17] This process exemplifies how non-viable wear debris can disrupt multicellular tissue homeostasis in the absence of infection. Aseptic inflammation and subsequent osteolysis represent two interconnected pathological stages in this cascade. Targeting these stages through pharmacological or biological interventions is a potential therapeutic strategy for mitigating both inflammatory activation and bone loss associated with aseptic loosing.[13,18–21]

Currently, cutting-edge research on aseptic loosening prevention mainly focuses on two strategic approaches: one involves the surface modification of artificial joints to significantly reduce the generation of wear particles,[22,23] while the other entails regulating cellular activities through biological interventions, such as gene silencing and targeted cell therapy.[7,20,21,24] While these strategies show promise, they require extensive preclinical and clinical evaluation to establish both efficacy and safety. A more practical and efficient way is to repurpose therapeutic agents already used in diseases sharing similar pathophysiological mechanisms. Chronic inflammation is a key pathological feature in multiple diseases, including atherosclerosis, osteoarthritis and rheumatoid arthritis.[25–28] Pharmacological modulation of inflammatory pathways has been well validated, and some natural compounds have demonstrated therapeutic potential in this regard.[29,30] Emodin (Emo), a hydrophobic trihydroxy-anthraquinone derived from Chinese herbs like rhubarb, is one such compound.[26,29] Accumulating evidence indicates that Emo exerts its anti-inflammatory effects by regulating signaling pathways, including NF-κB and PPARγ,[29,31,32] and can restore macrophage homeostasis under pathological conditions.[33] Calcitonin represents a well-established therapeutic option for treating osteoporosis and osteoarthritis.[34–36] This hydrophilic polypeptide hormone, secreted by parafollicular cells of the thyroid gland, plays a critical role in regulating calcium homeostasis and bone metabolism. It acts by binding to specific receptors on the osteoclast membrane, thereby inhibiting osteoclast motility and activation.[37] Salmon calcitonin (sCT), a structurally stable analog of human calcitonin, is often employed in clinical settings and has been explored in preliminary studies for managing bone complications after TJA.[38,39] Given their complementary mechanisms—Emo targeting inflammation and sCT counteracting excessive bone resorption—the combined use of Emo and sCT is a rational and promising strategy for preventing and treating aseptic loosening.

An effective drug delivery method constitutes another critical component of a potential therapeutic strategy, in addition to the selection of appropriate therapeutic agents. Conventional systemic administration is often limited by suboptimal drug concentrations at the lesion site and the risk of systemic adverse effects.[40,41] In contrast, local administration provides an effective alternative by increasing the therapeutic effect while reducing off-target toxicity, making it particularly suitable for treating localized diseases like aseptic loosening.[42–45] Injectable thermosensitive hydrogel systems based on amphiphilic block copolymers, such as poly(ethylene glycol) (PEG)-polyester copolymers,[46–52] PEG-poly(amino acid) copolymers,[53–57] and poly(phosphazenes),[58–60] have emerged as favorable platforms for localized delivery. These systems exhibit free-flowing sols at low or ambient temperature, enabling facile encapsulation of therapeutic payloads through simple mixing procedures.[49,61–63] Upon injection into the target site, they undergo a physiological temperature-induced sol–gel transition, forming *in situ* hydrogels loaded with drugs. Subsequently, the entrapped therapeutic agents are released continuously to the lesion region *via* mechanisms such as passive diffusion and/or degradation of the carrier polymer.[50,53,62,64,65] Thermosensitive poly(lactic acid-*co*-glycolic acid)-*b*-poly(ethylene glycol)-poly(lactic acid-*co*-glycolic acid) (PLGA–PEG–PLGA) hydrogels are particularly popular owing to their straightforward one-pot synthesis and well-documented biocompatibility.[49,50,58,64] Despite these advantages, achieving the localized and sustained co-delivery of multiple drugs at optimal dosages and desired ratios simultaneously from a single gel matrix remains highly challenging, particularly for drugs with markedly different physicochemical properties, like hydrophobic Emo and hydrophilic sCT.

In this study, we developed an injectable thermosensitive hydrogel system capable of enabling the sustained co-delivery of sCT and Emo for preventing wear particle-induced prosthesis aseptic loosening, as schematically presented in Fig. 1. A thermosensitive PLGA–PEG–PLGA hydrogel that exhibited a sol–gel transition in response to temperature elevation was selected as the delivery carrier. A two-step loading method was employed to enhance the loading efficiency and solubilization of hydrophobic Emo in the hydrogel matrix. For sustained release of the hydrophilic peptide sCT, it was first encapsulated into bovine serum albumin (BSA)-based nanoparticles (NPs), which were subsequently uniformly dispersed into the hydrogel matrix. The resulting hydrogel formulation containing both sCT-loaded NPs and Emo was denoted as sCT/Emo@Gel. The *in vitro* and *in vivo* release profiles of both agents were evaluated. Finally, a mouse bone-implanted air pouch model was created to assess the therapeutic efficacy of the sCT/Emo@Gel system.

2. Materials and methods

2.1. Materials

PEG with a molecular weight (MW) of 1500 (PEG1500), stannous octoate ($Sn(Oct)_2$), deuterated chloroform ($CDCl_3$), and BSA were purchased from Sigma-Aldrich (Missouri, USA). D,L-Lactide (LA) and glycolide (GA) were the products of Hangzhou Yueqian Biotechnology Co., Ltd. (Zhejiang, China). Emo was obtained from Adamas-beta (Shanghai, China). sCT was synthesized by Nanjing TGpeptide Biotechnology Co., Ltd (Jiangsu, China). All mobile phases, including tetrahydrofuran

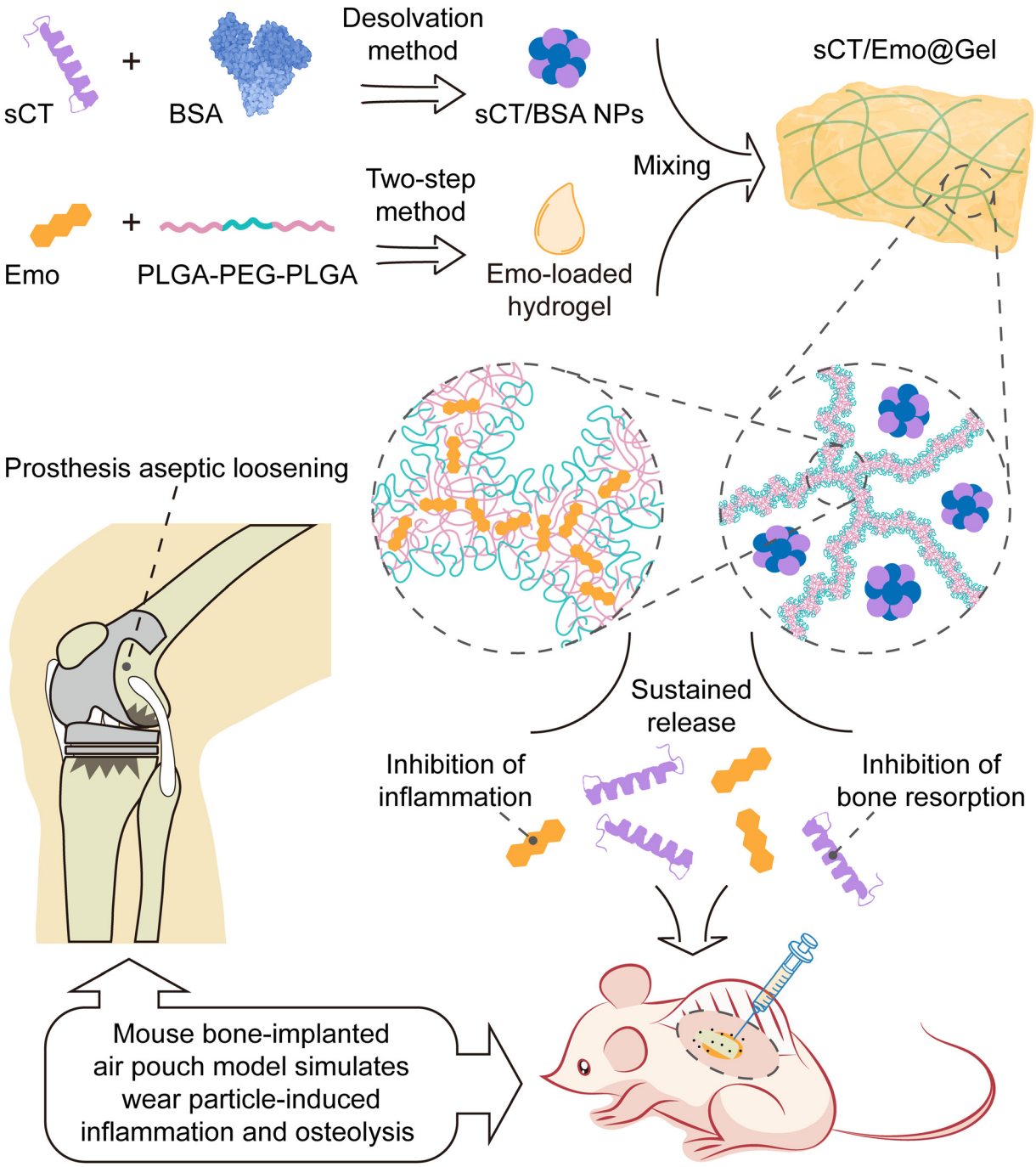

Fig. 1 Schematic illustration of the fabrication procedure of the sCT/Emo@Gel system and its *in vivo* mechanism of action. The injectable hydrogel prepared from amphiphilic PLGA–PEG–PLGA triblock copolymers exhibits a temperature-responsive sol–gel transition and forms a semi-solid hydrogel at body temperature. In the sol state, the system consists of a suspension of micelles self-assembled from the copolymer carriers, which serve as depots for the efficient solubilization of highly hydrophobic Emo. Upon thermal induction, these micelles percolate into a three-dimensional network, resulting in gelation. After local injection of the sCT/Emo@Gel system into the lesion site, the sustained release of Emo and sCT effectively inhibits aseptic inflammation and osteolysis, respectively.

(THF), acetonitrile and methanol, were bought from DiKMA (California, USA). Trifluoroacetic acid (TFA) was supplied by J&K Scientific (Beijing, China). Tween 80 and phosphate buffered saline (PBS, pH = 7.4) were acquired from Aladdin Scientific (Shanghai, China) and Sangon Biotech (Shanghai, China), respectively. All other reagents were purchased from Sinopharm Chemical Reagent Co., Ltd (Shanghai, China) and used without further purification.

2.2. Cells and animals

Two cell lines derived from mice, NIH/3T3 fibroblasts and RAW264.7 macrophages, were obtained from the Cell Bank of Chinese Academy of Science (Shanghai, China). NIH/3T3 cells were cultured in high glucose Dulbecco's modified Eagle medium (DMEM) containing 10% newborn calf serum (NBCS) and 1% penicillin–streptomycin (PS) at 37 °C with 5% CO_2. The culture medium for RAW264.7 cells consisted of DMEM supplemented with 10% fetal bovine serum (FBS), 1% PS and 1% sodium pyruvate. All reagents were the products of Gibco (New York, USA).

Male BALB/c mice aged 6 weeks were purchased from Shanghai Lab. Animal Research Center (Shanghai, China). The mice were raised in a clean environment at an appropriate temperature of about 23 °C with a 12-hour light/dark cycle. They were provided with standard laboratory diet and water *ad libitum*. All animal experiments were conducted in accordance with *Guide for the Care and Use of Laboratory Animals* (8th edition, National Academies Press, 2011) and approved by the Ethics Committee of the Laboratory Animal Center of Fudan University (202101006S).

2.3. Synthesis and characterization of PLGA–PEG–PLGA copolymers

PLGA–PEG–PLGA triblock copolymers were synthesized through ring-opening copolymerization of two cyclic monomers, LA and GA, in the presence of PEG1500 and $Sn(Oct)_2$ as the macromolecular initiator and catalyst, respectively. In brief, PEG1500 (15.00 g, 0.01 mol) was first transferred into a 250 mL three-necked flask and dried under vacuum with mechanical stirring at 120 °C for 1 h. While the flask was cooling to room temperature, LA (18.28 g, 0.127 mol), GA (14.72, 0.127 mol) and the toluene solution of $Sn(Oct)_2$ were added and stirred under vacuum at 90 °C for 0.5 h to remove any residual toluene and moisture. Under an argon atmosphere, the reaction was carried out at 150 °C with continuous stirring for 12 h. After the reaction, unreacted monomers in the mixture were eliminated by stirring under vacuum at 120 °C for 1 h. The crude product was then washed with water at 80 °C three times to remove water-soluble oligomers and residual PEG1500. Finally, the product was obtained by lyophilization with a yield of 76% and stored at −20 °C for subsequent use.

The chemical composition and MW of the synthetic copolymer were characterized by proton nuclear magnetic resonance (^{1}H NMR) using a 400 MHz Fourier transform-NMR spectrometer (AVANCE III HD, Bruker). The copolymer was dissolved in $CDCl_3$ containing tetramethylsilane as the internal standard.

The MW and molar-mass dispersity ($Đ_M$) value of the copolymer were confirmed using a gel permeation chromatography (GPC) system (1260, Agilent) installed with a refractive index detector. THF was employed as the mobile phase at a flow rate of 1.0 mL min^{-1} at 35 °C. Mono-disperse polystyrene standards were selected for calibration.

Microscopy images of the copolymer in water were acquired using a transmission electron microscope (TEM; Tecnai G20, FEI). A 1 wt% aqueous solution of the copolymer was prepared and incubated at a preset temperature for 10 min. Subsequently, the solution was dropped onto copper meshes, followed by drying in a temperature-controlled air bath maintained at the same temperature overnight prior to imaging. The acceleration voltage of the electron beam was set to 200 kV.

The hydrodynamic diameter (D_h) and size distribution of copolymer micelles in water were measured by dynamic light scattering (DLS) using a zeta-nano analyzer (Zetasizer Nano ZS90, Malvern) as a function of temperature. Before measurements, a 1 wt% aqueous copolymer solution was filtered through a 0.45 μm filter and equilibrated at each target temperature for 10 min. All DLS measurements were performed at a scattering angle of 90°.

2.4. Dynamic rheology measurement

Temperature-responsive rheological behaviors of copolymer aqueous solutions without or with drugs were measured using a dynamic rheometer (Kinexus Pro, Malvern) installed with a cone upper plate (1° cone angle and 60 mm diameter). 1.5 mL of sample was placed at the center of the lower plate, and the gap between the two plates was set to 0.03 mm. Low-viscosity silicone oil was applied to the edges of plates to prevent water evaporation. The temperature was initially set at 20 °C and increased to 40 °C at a rate of 0.5 °C min^{-1} with an oscillation frequency of 10 rad s^{-1}.

2.5. Loading of Emo in copolymer solution

The Emo-loaded thermosensitive hydrogel (Emo@Gel) was prepared using either a simple mixing method or a two-step method. The stability of the hydrogel solution and the encapsulation efficiency of Emo in micelles were compared.

For the simple mixing method, a calculated amount of Emo powder was directly added to a 25 wt% copolymer aqueous solution and mixed by magnetic stirring at 4 °C for over 72 h in a refrigerator, resulting in the formation of a hydrogel solution loading with 5 mg mL^{-1} Emo.

For the two-step method, a calculated amount of Emo powder and copolymer (1/50, w/w) were first dissolved together in a mixed solvent of ethanol and acetonitrile (volume ratio of 1 : 4) in an eggplant flask. Subsequently, the solvents were removed rapidly by rotary evaporation, leaving a uniform yellow Emo–copolymer mixture adhering to the flask wall. After that, deionized water was added in the required amount and stirred at 4 °C for over 72 h to form the Emo@Gel solution. Any trace organic solvents in the solution were further eliminated under vacuum with stirring at room temperature for 1 h.

2.6. Comparison of Emo@Gel prepared by different methods

For stability assessment, 2 mL of Emo@Gel solution was transferred into 5 mL glass vials and stored statically at 4 °C in the refrigerator. At predetermined time points, optical images of the samples were taken for visual inspection.

For the determination of the content of Emo in the micelles formed by PLGA–PEG–PLGA copolymers, 1 mL of Emo@Gel solution was transferred into 1.5 mL centrifuge tubes, and centrifuged at 2000*g* and 4 °C for 10 min. Next, 400 μL of the supernatant was gently aspirated using a pipette and transferred into a new tube. The supernatant was re-centrifuged under the same conditions to remove any free Emo in the solution. Finally, 100 μL of the secondary supernatant was taken off and diluted 100-fold with acetonitrile to completely dissolve the micelles and Emo therein. The concentration of Emo in the solution was determined by high performance liquid chromatography (HPLC), as described below.

2.7. Preparation of sCT/BSA NPs

BSA NPs without or with drugs were prepared by the desolvation method.[66,67] For the preparation of drug-free BSA NPs, BSA was first dissolved in deionized water, serving as the good solvent, to obtain a 4 mg mL^{-1} solution, and the pH of the solution was adjusted to the desired value using 1 M NaOH. Next, under high-speed magnetic stirring at over 1000 rpm, ethanol, acting as the poor solvent, was added dropwise into the BSA solution at a rate of 1 mL min^{-1} with the volume of ethanol being 2.5 times that of the BSA solution. Subsequently, ethanol in the suspension was removed through rotary evaporation. Finally, the NPs were gathered after lyophilization and stored at −20 °C for subsequent use. To determine the optimal pH for NP formation, BSA NPs were obtained from BSA aqueous solutions with different pH values for comparison.

For the preparation of sCT/BSA NPs, a series of mixture aqueous solutions containing sCT and BSA were desolvated following the procedure described above. The concentration of BSA was fixed at 4 mg mL^{-1}, while the weight ratios of sCT to BSA in the mixture solutions were set to 0.0625, 0.125, 0.25, 0.5, 1, 2, 4, 8 and 16.

2.8. Characterization of sCT/BSA NPs

The D_h of NPs in medium was measured by DLS. The NPs were redispersed evenly in deionized water at a BSA concentration of 1 mg mL^{-1} *via* ultrasound. Prior to measurement, the samples were filtered through 1.0 μm filters. Additionally, the zeta potentials of sCT (1 mg mL^{-1}), BSA (1 mg mL^{-1}) and different NPs in water were detected by electrophoretic light scattering (ELS) using the same instrument.

Microscopy images of NPs were acquired using TEM. The desolvated suspensions were dropped onto copper meshes and air-dried at room temperature overnight prior to observation.

The morphology of NPs was further examined using an atomic force microscope (AFM; multimode 8, Bruker). The desolvated suspensions were diluted 10-fold with a water–ethanol mixed solvent (volume ratio of 1 : 2.5), dropped onto the freshly exposed cleaved surface of mica sheets glued on iron sheets, and air-dried at room temperature overnight. A ScanAsyst-Air probe with a tip radius of 2 nm and a nominal spring constant of 0.4 N m^{-1} was used for scanning over a range of 1 μm × 1 μm × 5 μm on mica sheets. For comparison, aqueous solutions of free sCT and BSA were prepared at a concentration of 40 μg mL^{-1} and similarly observed.

The change in the secondary structure of sCT upon NP formation was analyzed using a circular dichroism (CD) spectrometer (Chirascan, Applied Photophysics). The NPs were redispersed evenly in deionized water at an sCT concentration of 1 mg mL^{-1}, while a free sCT solution was prepared under the same conditions. The scan range of wavelength was set from 200 nm to 260 nm with a bandwidth of 1 nm at a scanning rate of 1 nm s^{-1} at a temperature of 25 °C.

2.9. *In vitro* drug release

To fabricate sCT/Emo@Gel, a calculated amount of sCT/BSA NPs was added to the solution of Emo@Gel and stirred at 4 °C for 1 h. The sCT-loaded thermosensitive hydrogel (sCT@Gel) was prepared by directly mixing sCT with a 25 wt% copolymer aqueous solution under stirring at 4 °C for 1 h. The concentration of sCT was fixed at 1 mg mL^{-1} in both the sCT/Emo@Gel and sCT@Gel formulations.

For *in vitro* sCT release, 0.5 mL of sCT@Gel solution was accurately transferred into 15 mL test tubes with an inner diameter of 13.5 mm and equilibrated in the refrigerator at 4 °C overnight to remove bubbles. Subsequently, after being maintained at room temperature for 10 min, the tubes were incubated in a water bath at 37 °C for 10 min to form physical hydrogels. Finally, 5 mL of PBS containing 0.025 wt% NaN_3 was gently added into each tube as the release medium. The addition of NaN_3 was intended to prevent the presence of bacterial contamination that could interfere with the experiment. These tubes containing the samples were vertically immersed in a 37 °C water bath shaker at a shaking rate of 30 rpm. At predetermined time points, 2 mL of the release medium was withdrawn from each tube and then replaced with an equal amount of fresh medium. The collected release media were stored at −20 °C prior to analysis to prevent degradation.

For *in vitro* Emo release from Emo@Gel, the procedure of the experiment remained as described above. However, the release medium consisted of 15 mL of PBS containing 0.025 wt% NaN_3 and 0.5 wt% Tween 80. The addition of Tween 80 was intended to ensure the sink condition for drug release. At predetermined time points, 10 mL of the release medium was withdrawn from each tube and then replaced with an equal amount of fresh medium. The concentration of drug in release media was subsequently determined by HPLC.

2.10. Determination of drug concentration in release medium

Standard aqueous solutions of sCT were precisely prepared at various concentrations, while Emo was prepared as acetonitrile solutions. A HPLC system (e2695, Waters) equipped with a UV-Vis detector (2489, Waters) and a 4.6 mm × 250 mm C18 reversed phase column with a particle size of 5 μm (XBrigh BEH300, Waters) was employed for analysis. For sCT, the mobile phase was acetonitrile–ultrapure water (volume ratio gradually changing from 75 : 25 to 50 : 50 over 25 min) containing 0.1% TFA at a flow rate of 1.0 mL min^{-1} at 30 °C. For Emo,

the mobile phase was acetonitrile–ultrapure water (volume ratio of 85 : 15) at a flow rate of 1.0 mL min^{-1} at 30 °C. The optimal detection wavelengths for sCT and Emo were set to 220 nm and 222 nm, respectively. All samples were filtered through 0.45 μm filters before injecting into the HPLC system.

2.11. Cellular uptake of micelles

Leveraging the intrinsic fluorescence property of Emo, the cellular uptake of copolymer micelles was observed. Emo@Gel solution prepared by the two-step method was diluted 10-fold with cell culture medium and centrifuged at 2000*g* for 10 min. The supernatant was gently aspirated and filtered through 0.22 μm filters to obtain the culture medium containing Emo-loaded micelles (Emo@Micelles). NIH/3T3 cells or RAW264.7 cells were seeded in the 39 mm confocal dish with a 20 mm glass bottom at a density of 1×10^4 per dish and cultured in 1.0 mL of medium for 12 h. Next, the culture medium was replaced with fresh medium containing Emo@Micelles, and the cells were incubated for another 2 h. Subsequently, the medium was removed, and the cells were washed twice using PBS and fixed with 4% paraformaldehyde (PFA) solution for 5 min. After washing with PBS twice again, the cell nuclei were stained with 2-(4-amidinophenyl)-6-indolecarbamidine dihydrochloride (DAPI) solution for 1 min and washed twice with PBS. Finally, the cells were observed under a laser scanning confocal microscope (LSCM; C2+, Nikon) using tetramethylrhodamine (TRITC) and DAPI channels. The PFA and DAPI solutions were the products of Beyotime (Shanghai, China).

2.12. *In vivo* degradation and drug release of Emo@Gel

The mouse subcutaneous degradation model was adopted to monitor the *in vivo* Emo release behavior from Emo@Gel. Under continuous anesthesia with isoflurane gas, 0.2 mL of Emo@Gel solution was injected subcutaneously into the dorsal region of male BALB/c mice. The mice were sacrificed at predetermined time points, and the remaining hydrogels under the skin were collected and weighed. The collected hydrogels were subsequently dried by lyophilization and completely dissolved in 5 mL of a mixture of ethanol and acetonitrile (volume ratio of 1 : 1) *via* ultrasound. The obtained samples were filtered through 0.45 μm filters, and the concentration of Emo was determined by HPLC. The residual amount of Emo in the remaining hydrogel was further calculated.

2.13. Establishment of the wear particle-induced aseptic osteolysis mouse model

For simulating aseptic loosening of joint prosthesis, the mouse bone-implanted air pouch model was employed as the animal model of wear particle-induced aseptic inflammation and osteolysis. First, an air pouch was generated in male BALB/c mice. The dorsal skin of the mice was shaved completely and disinfected with 75% alcohol. Under continuous anesthesia with isoflurane gas, 6 mL of sterile air was injected subcutaneously into an indicated site on the dorsal region of the mice using a syringe equipped with a 0.22 μm filter to establish the air pouch. To maintain the pouch, 2 mL of sterile air was reinjected on Day 2, Day 4 and Day 6 post-establishment. On Day 7 after the formation of air pouch, a subset of mice was euthanized to serve as bone donors. The calvarias were harvested by surgical dissection, with adherent soft tissues carefully removed while preserving the periosteum. Each calvaria was divided along the sagittal suture into two pieces, each trimmed to about 10 × 5 mm with smooth edges and soaked in sterile normal saline (NS) before use. After anesthesia and disinfection, a 10 mm incision overlying the air pouch was created by a scalpel and a piece of calvaria was inserted into the pouch using forceps. 0.2 mL of sterile NS containing 1 wt% suspended titanium (Ti) particles was injected around the implanted bone to provoke inflammatory responses. As a control, 0.2 mL of sterile NS without particles was injected in some mice. The incision was closed with sutures, and 80 000 units of penicillin in 0.2 mL of NS were injected intraperitoneally to prevent infection. All procedures were performed under sterile conditions. The mice were placed in a warm environment until recovery. At the following day, the mice with particles were randomized into four groups (n = 6): Untreated, sCT@Gel, Emo@Gel and sCT/Emo@Gel. In the Untreated group, 0.2 mL of NS was injected subcutaneously around the implanted bone, while 0.2 mL of the corresponding formulation solution was injected in the other three groups. The mice without Ti particles served as the Sham group (n = 6) for comparison.

After 14 days of treatment, the mice were sacrificed for autopsy observation, micro-computed tomography (micro-CT) scanning and histological analysis. The implanted bone pieces along with the surrounding skin and muscle tissues, forming a three-layered "sandwich"-like structure, were harvested and fixed with 4% PFA solution for over 48 h.

2.14. Micro-CT imaging

The collected tissue specimens were scanned using a micro-CT imaging system (SkyScan 1176, Bruker) to observe the osteolysis of the implanted bone. The scanning parameters were set as follows: an X-ray source voltage of 45 kV and an image pixel size of 18 μm. After scanning, the 3D images of implanted bones were reconstructed using NRecom software (version 1.7.3, Bruker), DataViewer software (version 1.5.4, Bruker) and CTVox software (version 3.3.0, Bruker). Then, the bone volume to tissue volume ratio (percent bone volume, BV/TV), bone surface to volume ratio (BS/BV) and bone surface to tissue volume ratio (bone surface density, BS/TV) were determined using CTAn software (version 1.17.7, Bruker) within a cylindrical region of interest (ROI) measuring 2 mm × 2 mm × 1 mm.

2.15. Histological analysis

The collected tissue specimens were sequentially subjected to dehydration, decalcification, and paraffin embedding, followed by cutting into 6 μm sections. Hematoxylin–eosin (HE) staining, Masson's trichrome staining and tartrate-resistant acid phosphatase (TRAP) staining were implemented on the sections, respectively. High-resolution optical images of all stained slides were acquired using a research slide scanner

system (VS200, Olympus). The infiltrating cell number in the pouch membranes from HE staining slides was identified and counted using Image-Pro Plus software (version 6.0.0, Media Cybernetics) *via* selecting the specific color. The thickness of the pouch membranes in the HE staining slides, as well as the area and perimeter of implanted bone tissues in Masson slides were measured directly using OlyVIA software (version 3.22.0, Olympus).

2.16. Statistical analysis

All data were analyzed and visualized using Origin (version 10.2.0, OriginLab) and Graphpad Prism (version 9.5.1, Dotmatics), and the final results were expressed as mean ± standard deviation (SD). One-way ANOVA with Tukey's *post-hoc* test was performed to analyze the statistical significance among multiple groups. Statistical differences were marked as follows: "*" for $p < 0.05$, "**" for $p < 0.01$ and "***" for $p < 0.001$.

3. Results and discussion

3.1. Synthesis and characterization of the PLGA–PEG–PLGA copolymer and its hydrogel

A thermosensitive PLGA–PEG–PLGA triblock copolymer with a suitable MW and LA/GA molar ratio was synthesized *via* ring-opening copolymerization of GA and LA, initiated by PEG1500 and catalyzed by $Sn(Oct)_2$ (Fig. 2A). The molecular parameters of the synthetic copolymer were designed based on a previous study[64] and confirmed by GPC and ^{1}H NMR. The retention time of the synthetic copolymer in GPC was markedly shorter than that of the macroinitiator PEG1500 (Fig. 2B), and the trace showed a unimodal distribution with a $Đ_M$ value of 1.22, indicating the successful synthesis of the desired product. Furthermore, four characteristic peaks corresponding to the PLGA–PEG–PLGA copolymer were identified in the ^{1}H NMR spectrum at 1.55 ppm (–COCH(CH_3)O–, e), 3.65 ppm (–CH_2CH_2O–, d), 4.80 ppm (–COCH_2O–, b), and 5.10 ppm (–COC*H*(CH_3)O–, a) (Fig. 2C). By integrating these peaks, the number-average MW (M_n) and the LA/GA molar ratio of the synthetic copolymer were calculated. The basic parameters of the synthetic copolymer are summarized in Table 1.

The synthetic PLGA–PEG–PLGA copolymer could be dissolved in water at low and room temperature, and its concentrated aqueous solution underwent a sol–gel transition with an increase of temperature, resulting in the formation of a non-flowing physical hydrogel at body temperature. The temperature-responsive gelation mechanism of the PLGA–PEG–PLGA hydrogel is attributed to the thermally induced formation of a percolated network of micelles,[58,68] as illustrated in Fig. 2A. This mechanism has been experimentally confirmed *via* TEM and DLS observations. As presented in Fig. 2D, the PLGA–PEG–PLGA copolymers self-assembled into spherical micelles at ambient temperature, which further aggregated into an interconnected three-dimensional network structure at physiological temperature. DLS measurements also disclosed the aggregation of copolymer micelles with increasing temperature (Fig. S1).

3.2. Solubilization of Emo in copolymer solution

Emo is a very hydrophobic anthraquinone compound with extremely low solubility in water, quantified at less than 0.2 μg mL^{-1} by HPLC. One promising strategy to enhance the solubility of hydrophobic molecules is the use of nanoscale carriers, such as liposomes, micelles, or vesicles.[69–72] The micelles formed by thermosensitive PLGA–PEG–PLGA copolymers can effectively solubilize various hydrophobic drugs.[47,48] However, we found that the Emo@Gel solution prepared using the simple mixing method was unstable even after continuous stirring for three days. The sediment at the bottom of the bottle indicated that the majority of Emo molecules were not solubilized into the micelles (Fig. 3B). To address this issue, we employed a two-step loading strategy to prepare the Emo@Gel solution. As illustrated in Fig. 3A and S2, Emo and PLGA–PEG–PLGA copolymers were first dissolved in a mixed solvent of ethanol and acetonitrile, followed by solvent removal *via* rotary evaporation. Finally, the resulting mixture was dissolved in water to obtain the desired Emo@Gel solution. After a long period of standing, the Emo@Gel solution prepared by the two-step method remained homogeneous without any sedimentation (Fig. 3B).

Quantitative analysis revealed that the simple mixing method only solubilized 0.05 mg mL^{-1} of Emo into the 25 wt% PLGA–PEG–PLGA solution. In contrast, the two-step strategy achieved a remarkable 70-fold increase in Emo solubility, reaching 3.54 mg mL^{-1} in the 25 wt% PLGA–PEG–PLGA solution (Fig. 3C). In addition, leveraging the intrinsic fluorescence property of Emo, the cellular uptake of Emo@Micelles was confirmed *via* LSCM. As shown in Fig. 3D, intense red fluorescence of Emo was observed in both NIH/3T3 cells and RAW264.7 cells after 2 h of co-culture, suggesting that the PLGA–PEG–PLGA micelles loaded with hydrophobic Emo could efficiently enter the cells *via* endocytosis. This is crucial for exerting the therapeutic effect of Emo.

3.3. Preparation and evaluation of sCT/BSA NPs

sCT is a polypeptide hormone composed of 32 amino acid residues and exhibits high solubility in water. Therefore, it is foreseeable that sCT may undergo rapid release from a hydrogel depot. Considering that the isoelectric point (PI) of sCT is 9.3, it carries a positive charge at physiological pH. Previous studies have shown that leveraging electrostatic interactions between carriers and drugs represents a viable strategy for modulating the release kinetics of protein- and peptide-based drugs.[34,62,73] BSA, with a PI of 4.7, is negatively charged under physiological conditions and has been widely recognized as a biocompatible and reliable carrier material for drug delivery.[74] Based on these considerations, we prepared sCT/BSA composite NPs to mitigate the initial burst release of sCT and prolong its release duration from the PLGA–PEG–PLGA hydrogel.

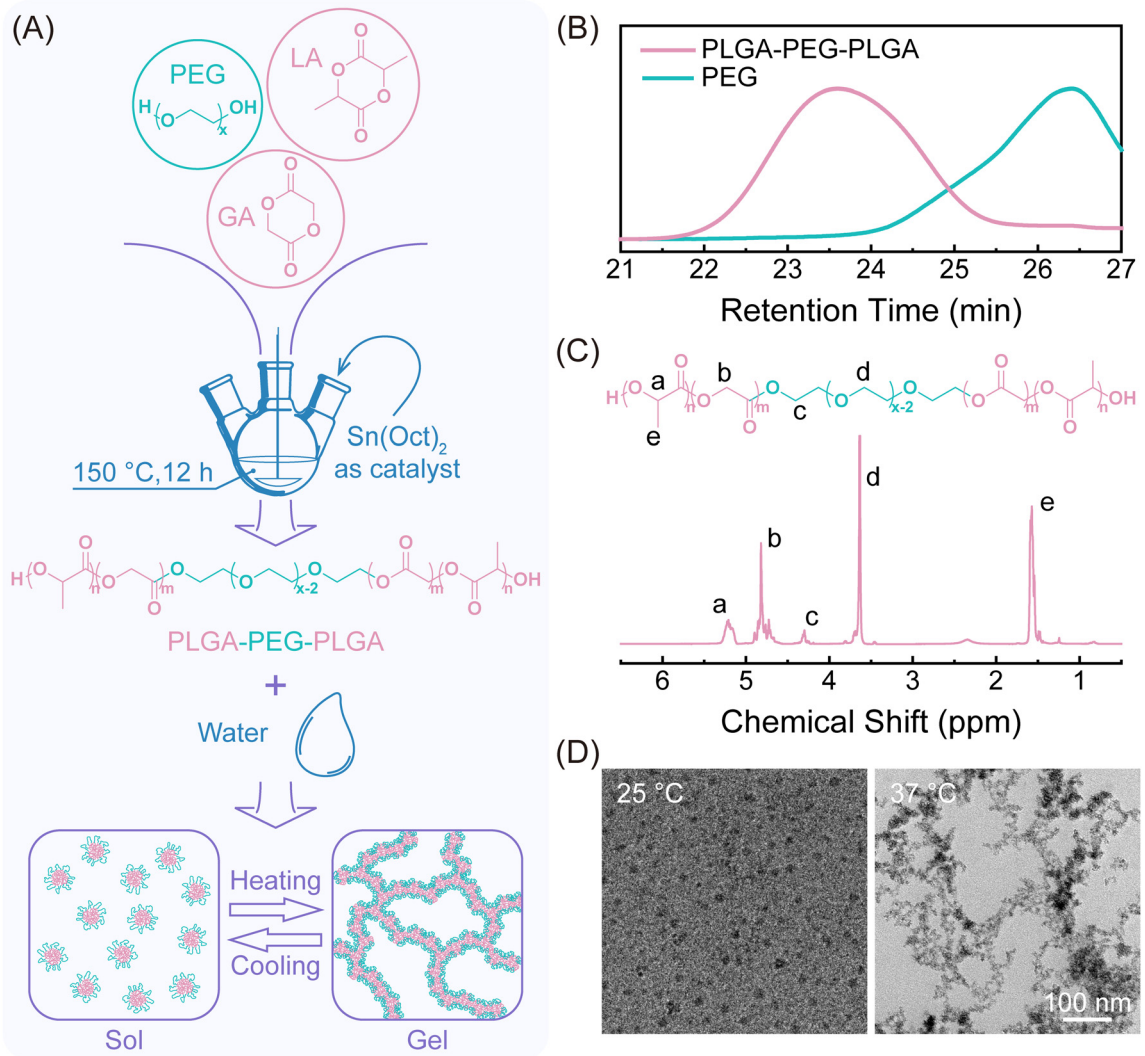

Fig. 2 Synthesis and characterization of the PLGA–PEG–PLGA copolymer. (A) Synthesis route of the PLGA–PEG–PLGA triblock copolymer and schematic representation of the temperature-responsive gelation process of the copolymer/water system. (B) GPC traces of the synthesized copolymer and PEG1500. (C) ^{1}H NMR spectrum of the synthesized copolymer in $CDCl_3$. (D) TEM images of PLGA–PEG–PLGA copolymers in water (1 wt%) at 25 °C and 37 °C.

Table 1 Basic characteristics of the PLGA–PEG–PLGA copolymer

M_n [a]	M_n [b]	$Đ_M$ [b]	LA/GA[a] (mol mol^{-1})	T_{gel} [c] (°C)
1890-1500-1890	5040	1.22	1 : 1	35.6

[a] Calculated *via* ^{1}H NMR, according to the M_n of the middle block PEG provided by Sigma-Aldrich. [b] Confirmed by GPC. [c] Determined by dynamic rheological analysis using 25 wt% copolymer aqueous solution.

sCT/BSA NPs and drug-free BSA NPs were prepared through a desolvation method using ethanol as the poor solvent (Fig. 4A and S3). This is a classical method for the preparation of NPs.[74,75] The key parameters—such as the concentration of BSA aqueous solution, the ethanol content, the rate of ethanol addition and the stirring speed—were selected in reference with previous studies.[66,67] Since the pH of BSA aqueous solution is known to significantly influence the size of BSA NPs,[67,75] and might affect the charged states of BSA and sCT in their mixture solutions, BSA NPs without sCT were first prepared under different pH conditions to determine the optimal parameters. We found that a pH of 10 yielded the smallest particle size—around 200 nm (Fig. 4B)—making it the optimal choice. Additionally, maintaining a pH of 10 can prevent premature aggregation of BSA and sCT in the aqueous solution before desolvation, as both molecules carry a negative charge under this condition. For this reason, in all subsequent experiments, the pH of the solutions of BSA and sCT was adjusted to 10.

Subsequently, a series of sCT/BSA NPs with varying weight ratios were prepared, and their hydrodynamic sizes and zeta potentials were measured using a Zeta-nano analyzer. As the

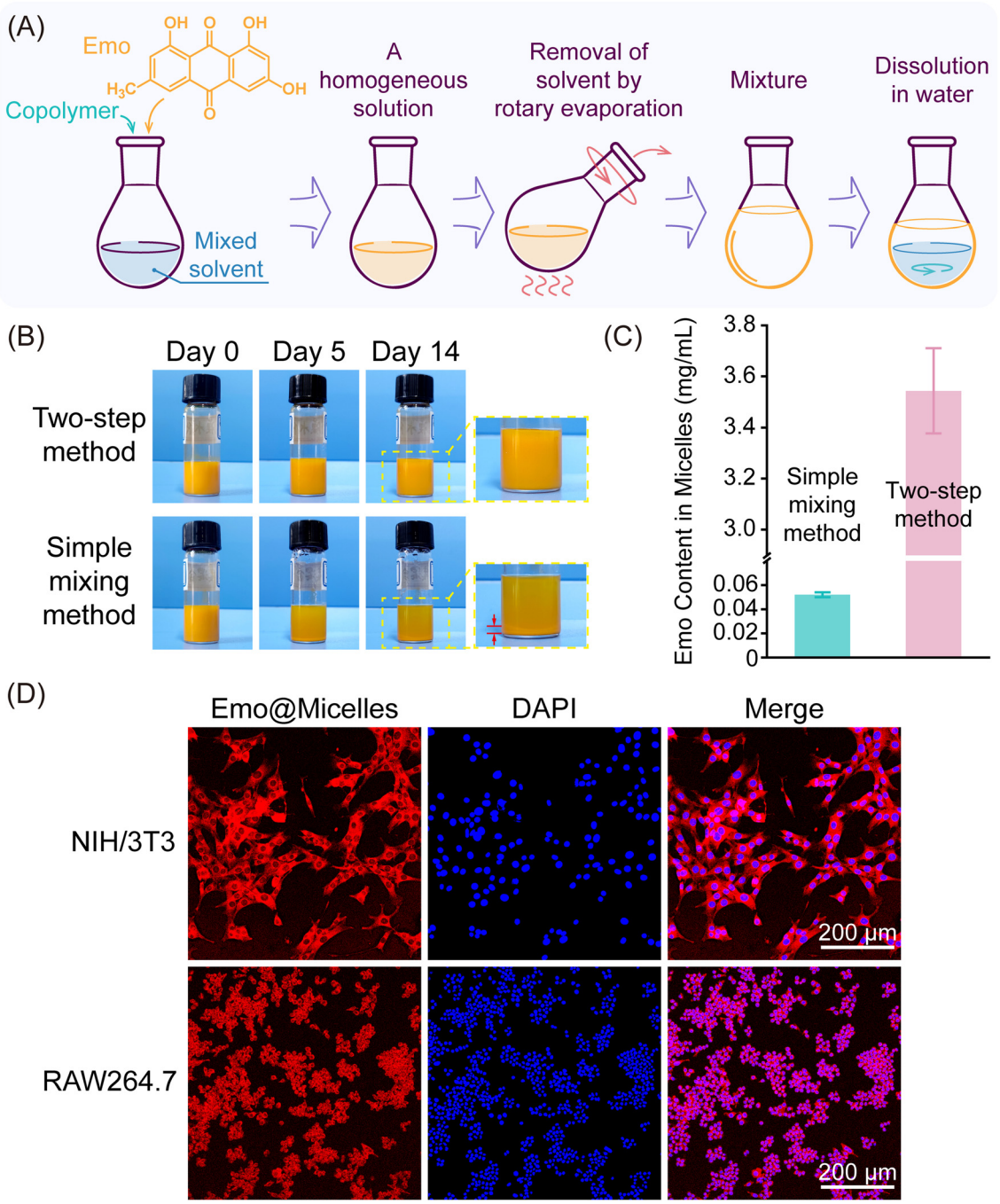

Fig. 3 Loading of Emo in copolymer solution. (A) Schematic diagram of the two-step method for fabricating Emo@Gel. (B) Stability assessment of Emo@Gel obtained by different methods over time. Optical images were taken at indicated time points. (C) Emo content in micelles of Emo@Gel prepared by different methods. Error bars denote the SD of data (n = 3). (D) Cellular uptake of Emo@Micelles. The sample was incubated with NIH/3T3 cells or RAW264.7 cells for 2 h.

content of sCT increased within the NPs, the zeta potential shifted gradually from about −70 mV for BSA NPs without sCT to positive values (Fig. 4C). Previous studies have demonstrated that complexes formed *via* electrostatic interactions tend to be most stable when approaching charge neutrality.[76,77] Thus, the point at which the zeta potential neared neutrality indicated the optimal balance between sCT and BSA—corresponding to a weight ratio of 4 in our experiments. When the ratio exceeded 4, the resulting sCT/BSA NPs exhibited a positive charge comparable to that of free sCT, suggesting full saturation of BSA's binding capacity.

Changes in the zeta potential reflect how the surface charge density of the sCT/BSA complexes varies with composition. According to the Gouy–Chapman model of the electrical

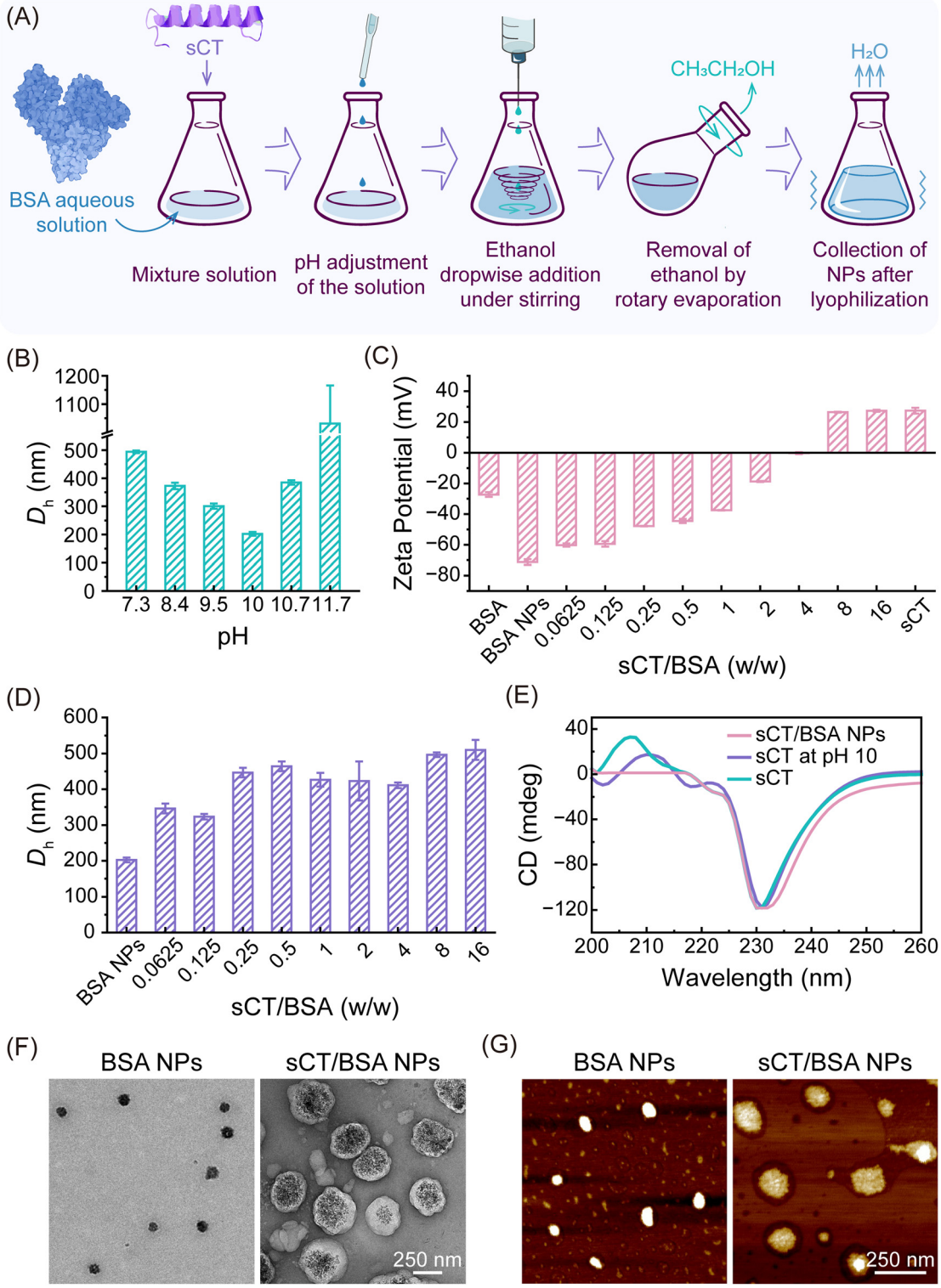

Fig. 4 Preparation and characterization of sCT/BSA NPs. (A) Schematic diagram of the desolvation method for preparing sCT/BSA NPs. (B) Particle sizes of BSA NPs formed under different pH conditions. (C) Zeta potentials and (D) particle sizes of sCT/BSA NPs at different weight ratios. Error bars denote the SD of data (n = 3). (E) CD spectra of sCT and sCT/BSA NPs at a weight ratio of 4. (F) TEM and (G) AFM images of BSA NPs and sCT/BSA NPs at a weight ratio of 4.

double-layer structure, the surface charge density (σ) can be calculated using the following equation:[78]

$$\sigma = \sqrt{8\varepsilon_{r,water}\varepsilon_0 N_A k_B T c}\sinh\left(\frac{ze\zeta}{2k_B T}\right) \quad (1)$$

Since the measurements were performed in deionized water, the zeta potential (ζ) was used as a close approximation of the surface potential (ψ_0), and the ion concentration (c) and valence (z) were taken as 1×10^{-4} mol m^{-3} and 1, respectively. The resulting surface charge densities of the NPs are summarized in Table S1. Interestingly, we observed a linear relationship between the surface charge density and the sCT weight fraction (W_{sCT}) in the NPs (Fig. S4), which helps us better understand how each component contributes to the overall surface properties. This relationship can be described by the following equation:

$$\sigma = (\sigma_{sCT} - \sigma_{BSA})W_{sCT} + \sigma_{BSA} \quad (2)$$

Here, σ denotes the surface charge density of NPs, and σ_{sCT} and σ_{BSA} represent the contributions per unit mass of sCT or BSA, respectively, to the surface charge density. Based on the linear fitting shown in Fig. S4, the values of σ_{sCT} and σ_{BSA} were determined to be 2.09×10^{-5} and -6.22×10^{-5} C m^{-2}, respectively. These values are in good agreement with the experimentally measured surface charge densities of pure sCT and BSA NPs. According to the fitted curve, the optimal sCT weight fraction was 0.749, corresponding to an sCT/BSA weight ratio of approximately 3. With this insight, sCT/BSA NPs with weight ratios of 2 and 4 were chosen for further comparison in subsequent experiments.

The hydrodynamic size of BSA NPs without sCT was about 200 nm. Following the addition of sCT, the particle size initially increased and subsequently stabilized within the range of 400–500 nm (Fig. 4D). This gradual growth suggests a well-controlled assembly process as the two components interact. TEM observations further revealed that sCT-free BSA NPs had an average size of approximately 100 nm, while sCT/BSA NPs at the weight ratio of 4 reached about 300 nm (Fig. 4F). Even smaller dimensions were observed by AFM scanning (Fig. 4G and S5). The sizes observed by TEM and AFM were consistently smaller than those measured by DLS—this difference is understandable, as TEM and AFM analyze samples in a dried state, whereas DLS measures particles in solution, including their hydration layer. Finally, CD analysis confirmed that the secondary structure of sCT remained unaltered after short-term exposure to alkaline conditions (pH 10) and in the resulting sCT/BSA NPs (Fig. 4E and Table S2), indicating that its biological activity—and thus therapeutic potential—is well preserved throughout the preparation process.

3.4. Temperature-responsive gelation properties of hydrogels with or without drugs

The sol–gel transition behaviors of PLGA–PEG–PLGA hydrogels with or without drugs were monitored using a dynamic rheometer (Fig. 5A and B). At low or room temperature, all systems exhibited low values of storage modulus (G') and loss modulus (G''), with G'' exceeding G', indicating a low-viscosity and injectable sol state. As the temperature increased, both G' and G'' increased sharply, and the increase rate of G' was faster than that of G''. The temperature at which G' surpasses G'' is generally regarded as the sol–gel transition temperature (T_{gel}).[79] According to this criterion, the T_{gel} values of the drug-free PLGA–PEG–PLGA hydrogel (Blank Gel), sCT/Emo@Gel, sCT@Gel and Emo@Gel were determined to be 35.6 °C (Table 1), 34.7 °C, 35.6 °C and 34.5 °C, respectively, confirming that all formulations can form physical hydrogels at physiological temperature. The incorporation of sCT/BSA NPs had a negligible influence on the temperature-induced sol–gel transition of the copolymer aqueous solution. However, the introduction of Emo led to a 1 °C decrease in T_{gel}. This phenomenon can be attributed to the increased hydrophobicity of the micelles caused by Emo, which promotes micelle aggregation upon heating.[68] Additionally, the sCT/Emo@Gel system maintained a thermoreversible sol–gel transition process (Fig. 5C), which facilitated its *in vivo* applications.

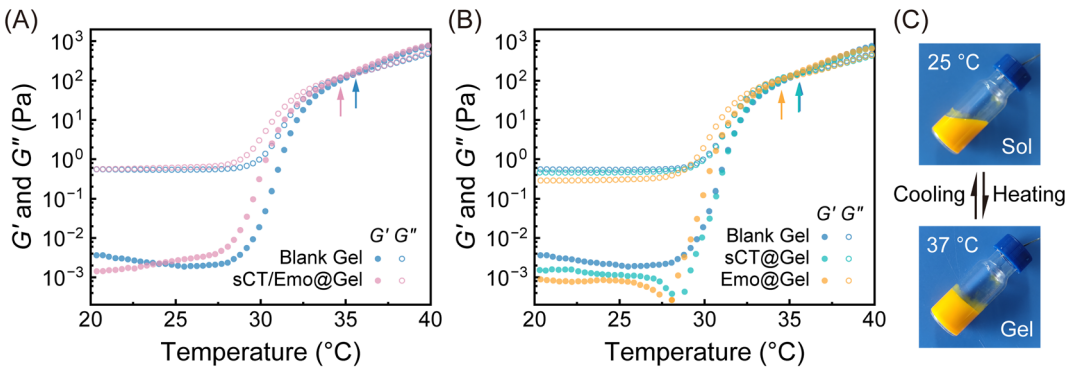

Fig. 5 Temperature-dependent sol–gel transitions of hydrogels with or without drugs. (A) Rheological curves of Blank Gel and sCT/Emo@Gel as a function of temperature. (B) Rheological curves of Blank Gel, sCT@Gel and Emo@Gel as a function of temperature. (C) Optical images of the sCT/Emo@Gel system at 25 °C and 37 °C. The arrows denote the T_{gel} values of the systems marked by the corresponding colors. The polymer concentration was 25 wt%.

3.5. *In vitro* and *in vivo* drug release

The *in vitro* release profiles of sCT and Emo from the thermosensitive PLGA–PEG–PLGA hydrogel were evaluated, and HPLC was employed for the detection of the two drugs (Fig. S6 and S7). We first compared sCT release behaviors from the hydrogel encapsulating two types of sCT/BSA NPs with different weight ratios and free sCT. The sCT/BSA NPs at the weight ratio of 4 significantly reduced the initial burst release of sCT (21.4 ± 3.6%) on the first day compared to free sCT (32.5 ± 3.7%) and the sCT/BSA NPs at the weight ratio of 2 (32.1 ± 3.3%) (Fig. 6A and B). Meanwhile, the introduction of sCT/BSA NPs at the weight ratio of 4 enabled the sustained release of sCT for three weeks (Fig. 6A). These favorable results are attributed to the appropriate electrostatic interaction between BSA and sCT, which effectively suppressed the diffusion of sCT. Therefore, the weight ratio of 4 was reconfirmed as the optimal ratio for sCT/BSA NPs in the sCT/Emo@Gel system.

For Emo, a linear release profile was observed in both *in vitro* and *in vivo* experiments (Fig. 6C and D). The change in the residual mass of Emo within the hydrogel matrix was largely consistent with the weight loss of the hydrogel, indicating that the degradation of the hydrogel controlled the release of Emo. In sum, these results demonstrate that the thermosensitive PLGA–PEG–PLGA hydrogel system has the ability to sustainably deliver the two drugs with distinct properties.

Before *in vivo* application, it is worth noting that the biocompatibility of the PLGA–PEG–PLGA hydrogel has been confirmed in previous research studies *via in vitro* cytotoxicity assays, and *in vivo* degradation and bio-safety evaluations.[64,80] More importantly, both blocks of the copolymer—PEG and PLGA—have been approved for *in vivo* use for decades.

3.6 Inhibition effects of sCT/Emo@Gel on aseptic inflammation and osteolysis

The *in vivo* preventive efficacy of the sCT/Emo@Gel system was evaluated using a mouse bone-implanted air pouch model (Fig. 7A). This pathological model could be conveniently established on small animals without long-time waiting and high cost, and it is modified on the basis of the mouse subcutaneous air pouch model, a classic animal model for chronic inflammation.[81] In this model, after the stable formation of the subcutaneous air pouch, fibroblasts and macrophages infiltrate into the connective tissue (superficial fascia) under the skin, forming a fibrous layer known as the pouch membrane.[82] Histological analysis revealed a gradual increase in the thickness of the pouch membrane over the maintenance time of the air pouch (Fig. S8). The cellular infiltration and inflammatory mediators observed in the pouch membrane under wear particle stimulation are analogous to the aseptic inflammatory responses of synovial tissue in the joint cavity associated with periprosthetic osteolysis.[81] Therefore, by implanting homologous bone within the air pouch, the model can reproduce the pathological features of inflammation-induced periprosthetic osteolysis to the greatest extent.

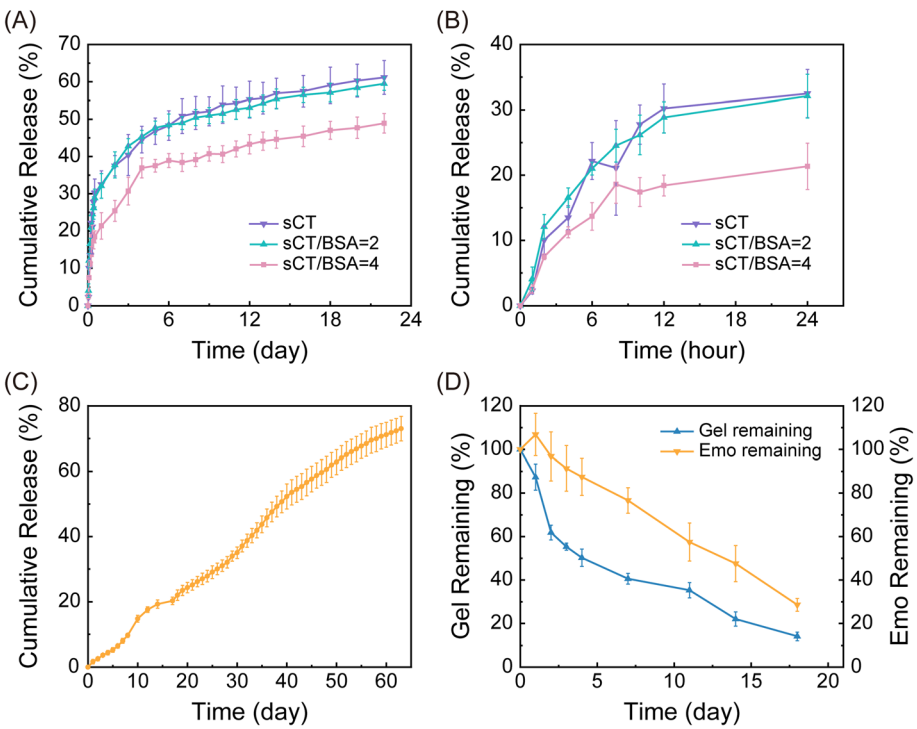

Fig. 6 *In vitro* and *in vivo* drug release profiles. (A and B) *In vitro* release curves of sCT from various hydrogel formulations in PBS (pH = 7.4) at 37 °C (n = 3). (C) *In vitro* release curve of Emo from Emo@Gel in PBS (pH = 7.4) at 37 °C (n = 4). (D) Changes in the weight percentage of the remaining Emo and the remaining hydrogel matrix as a function of time after subcutaneous injection of Emo@Gel (n = 4). Error bars denote the SD of data.

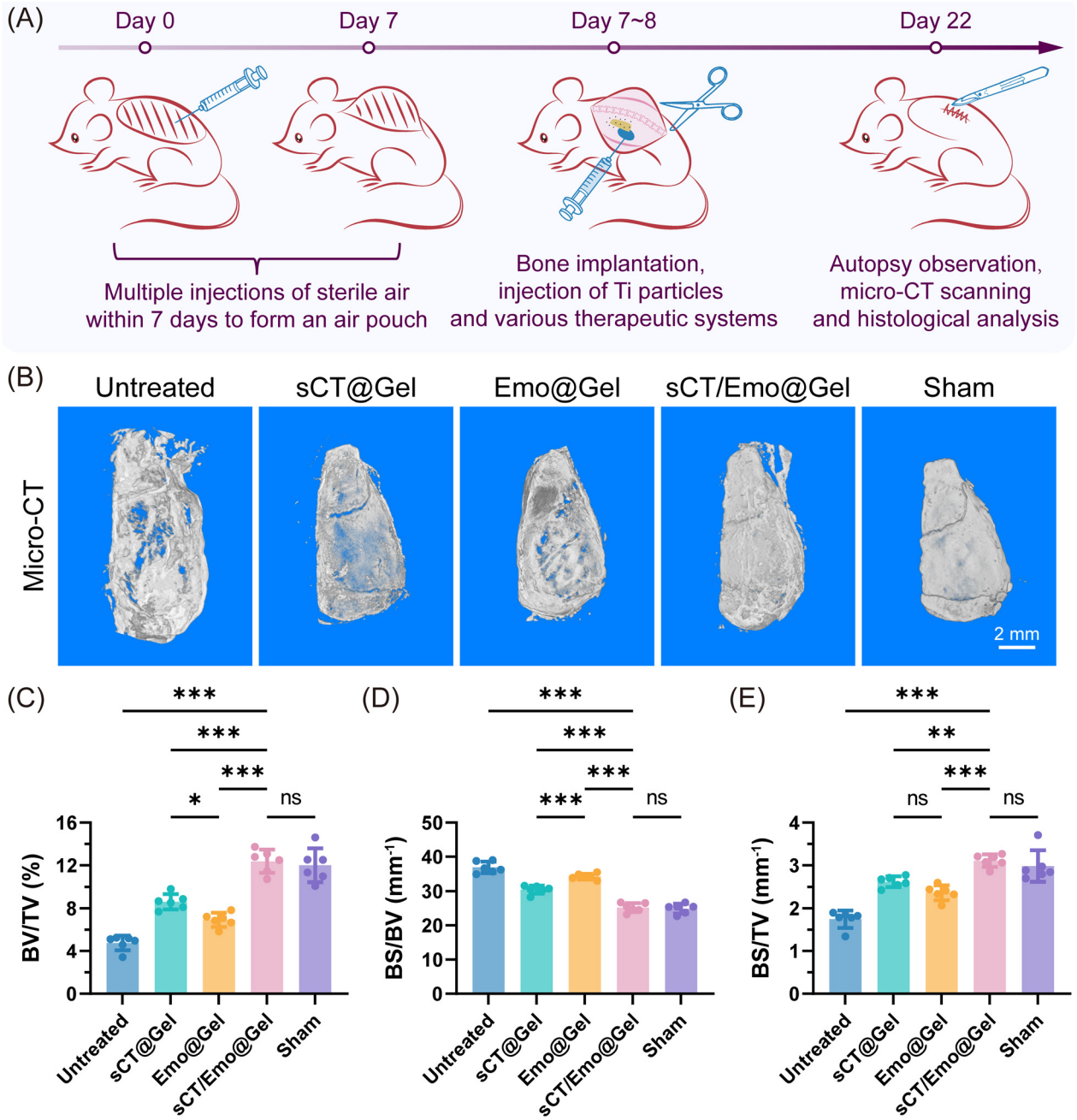

Fig. 7 Preventive efficacy *in vivo*. (A) Schematic diagram of the establishment of the mouse model and the subsequent treatment schedule. (B) Representative 3D reconstruction images of implanted bones after 14 days of treatment. Statistical analysis of (C) BV/TV, (D) BS/BV and (E) BS/TV based on micro-CT images in each group. Error bars denote the SD of data (n = 6).

After the model was established, the mice were subjected to various interventions, and no infections were observed in any of the animals during the experiment period. After 14 days of treatment, all mice were euthanized, and the implanted bones were harvested for further analysis. Bone loss is the direct cause of prosthesis loosening; therefore, analyzing the osteolysis of the implanted bones can visually demonstrate the preventive efficacy of different formulations. Micro-CT observations showed severe osteolysis in the Untreated group under Ti particle stimulation (Fig. 7B). Conversely, the administration of sCT/Emo@Gel prominently reduced bone resorption, with intact bone pieces observed in the sCT/Emo@Gel group, similar to those in the Sham group. This result indicates that the sCT/Emo@Gel system can effectively inhibit aseptic loosening. In both sCT@Gel and Emo@Gel groups, mild osteolysis was observed, with the degree of osteolysis being lower in the sCT@Gel group compared to that in the Emo@Gel group. For this phenomenon, we speculate that the direct inhibitory

effect of sCT on osteoclast activity may be more beneficial for reducing osteolysis within a short timeframe.

Subsequently, three morphometric parameters reflecting the osteolysis degree were quantified (Fig. 7C–E). In ROIs with similar sized bone samples, a higher bone content corresponds to a larger BV/TV value. Increased porosity due to osteolysis raises the BS while reducing the BV, resulting in a higher BS/BV ratio. The BV/TV and BS/TV values in the sCT/Emo@Gel

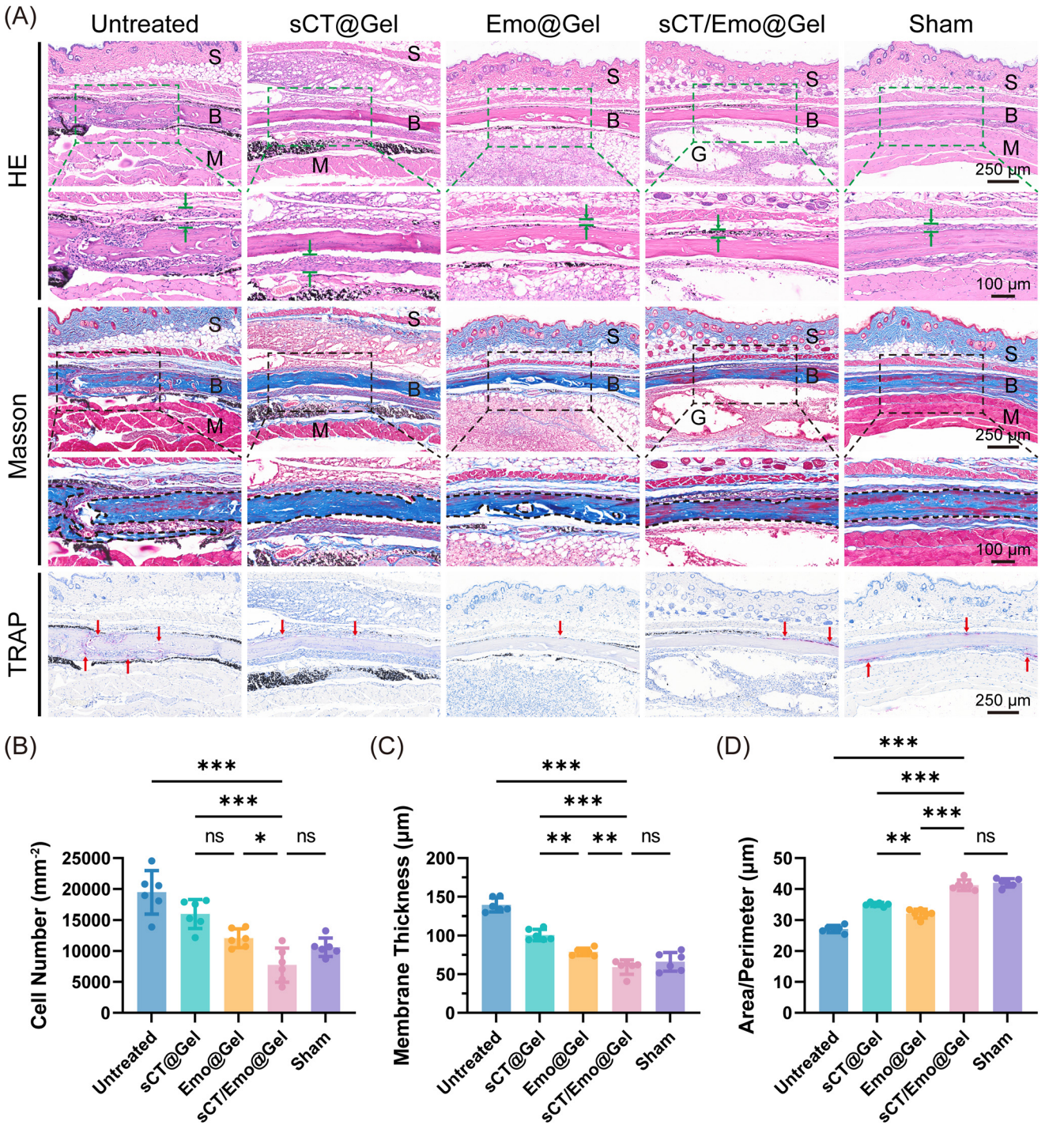

Fig. 8 Histological analysis. (A) Representative histological section images of bone-implanted pouch "sandwich"-like tissues stained with HE, Masson's trichrome and TRAP. Green arrows in the HE-stained slides indicate the pouch membranes. Black dashed lines in the Masson-stained slides delineate the borders of implanted bones. Red arrows in the TRAP-stained slides denote TRAP-positive regions. S: sink, B: implanted bone, M: muscle, and G: residual hydrogel. Statistical analysis of (B) the number of infiltrating cells per mm^2, (C) the thickness of the pouch membrane, and (D) the area-to-perimeter ratio values of the implanted bones in various groups. Error bars denote the SD of data (n = 6).

group were 11.2 ± 1.0% and 3.0 ± 0.2 mm^{-1}, respectively, which were evidently higher compared to those in the Untreated group (4.8 ± 0.7% and 1.7 ± 0.2 mm^{-1}), the sCT@Gel group (8.6 ± 0.7% and 2.6 ± 0.1 mm^{-1}) and the Emo@Gel group (6.9 ± 0.7% and 2.4 ± 0.2 mm^{-1}), and similar to those in the Sham group (10.7 ± 1.0% and 2.9 ± 0.3 mm^{-1}). In addition, the BS/BV values in the sCT/Emo@Gel group (26.7 ± 1.7 mm^{-1}) and the Sham group (27.4 ± 1.4 mm^{-1}) were lower than those in the other three groups (36.9 ± 1.7 mm^{-1} in the Untreated group, 30.5 ± 1.2 mm^{-1} in the sCT@Gel group and 34.2 ± 0.8 mm^{-1} in the Emo@Gel group). These findings indicate that the sCT/Emo@Gel system exhibits the best *in vivo* preventive efficacy against osteolysis.

The therapeutic efficacy of sCT/Emo@Gel was further determined through histological analysis (Fig. 8A). The harvested bone-implanted pouch tissue, consisting of skin, the implanted bone and muscle, formed a "sandwich"-like structure (Fig. S9 and S10). The inflammation responses in the tissues, mainly within the pouch membrane, were assessed *via* HE staining. As shown in Fig. 8A, a large amount of Ti particles, appearing as black dots, were retained surrounding the implanted bone in all groups except the Sham group. In the Untreated group, extensive cell infiltration into the pouch tissue around the implant bone was observed, indicating a severe inflammation response induced by Ti particles. This infiltration provoked the hyperplasia of the pouch membrane, and even led to cell invasion into gaps between bone tissue parts after osteolysis. In contrast, the degree of cellular invasion and pouch membrane hyperplasia was mitigated after treatment with sCT/Emo@Gel, sCT@Gel or Emo@Gel. For comparison, the number of infiltrating cells and the thickness of the pouch membrane were quantified. As presented in Fig. 8B and C, the infiltrating cell number per mm^2 was 10 609 ± 1489 in the Sham group, 7723 ± 2769 in the sCT/Emo@Gel group, 12 075 ± 1513 in the Emo@Gel group, 15 966 ± 2333 in the sCT@Gel group and 19 473 ± 3519 in the Untreated group. The pouch membrane thickness was 66 ± 12 μm in the Sham group, 59 ± 9 μm in the sCT/Emo@Gel group, 79 ± 5 μm in the Emo@Gel group, 101 ± 7 μm in the sCT@Gel group and 139 ± 9 μm in the Untreated group. Specifically, the sCT/Emo@Gel system showed the lowest degree of inflammatory response, close to that of the Sham group. Treatment with Emo@Gel also significantly inhibited inflammation, and outperformed the treatment with sCT@Gel. These findings confirm that the sCT/Emo@Gel system has the best inhibition effect on wear particle-induced aseptic inflammation.

The morphology of the implanted bones was also observed *via* Masson's trichrome staining (Fig. 8A). Using this staining method, collagen in bone tissues and pouch membranes is stained blue, while muscle tissue is stained red. In the Sham group, the bone tissue had smooth and well-defined borders, and the collagen fibers were arranged tightly (Fig. S9). In contrast, in the Untreated group, collagen fibers became loose and dispersed, and the bone tissue displayed irregular and elongated borders due to severe osteolysis (Fig. S10). Therefore, the degree of osteolysis is positively correlated with the area-to-perimeter ratio of the bone. We calculated the area-to-perimeter ratio values of the implanted bones. As displayed in Fig. 8D, the sCT/Emo@Gel group exhibited an area-to-perimeter ratio value of 41.2 ± 1.7 μm, closely resembling that of the Sham group at 42.0 ± 1.4 μm. The values for the sCT@Gel group (35.0 ± 0.6 μm) and Emo@Gel group (32.0 ± 1.4 μm) were remarkably higher than that of the Untreated group (27.1 ± 1.1 μm), but inferior to that of the sCT/Emo@Gel group. These results were consistent with the analysis of micro-CT images (Fig. 7B–E), and confirmed that treatment with sCT/Emo@Gel achieved the best inhibitory effect on osteolysis.

Finally, we inspected the distribution of osteoclasts in tissue sections *via* TRAP staining (Fig. 8A), a method that highlights TRAP—an enzyme specific to osteoclasts—with a distinct purple color. A large number of purple-stained regions were observed in the Untreated group, suggesting heightened osteoclast activity and severe osteolysis, which is a direct consequence of aseptic inflammation. In contrast, the TRAP-positive regions were lessened in the other four groups.

4. Conclusions

In this study, we exploited a local and long-acting co-delivery system of Emo and sCT based on an injectable and thermosensitive PLGA–PEG–PLGA hydrogel for preventing wear particle-induced aseptic loosening. The highly hydrophobic Emo was effectively solubilized into the micelles formed by the carrier polymers in water. sCT/BSA NPs with the optimal weight ratio were fabricated, and the electrostatic interaction between BSA and sCT significantly reduced the initial burst release of sCT and extended its release period from the hydrogel matrix. The incorporation of Emo and sCT/BSA NPs did not significantly interfere with the sol–gel transition behavior of the PLGA–PEG–PLGA hydrogel, and the resulting sCT/Emo@Gel system achieved simultaneous and continuous release of the two agents with distinct water solubility. A mouse bone-implanted air pouch model was created to mimic the pathological features of wear particle-induced periprosthetic osteolysis, and a single local administration of sCT/Emo@Gel significantly inhibited aseptic inflammation and osteolysis induced by Ti particles. This is ascribed to the sustained release of anti-inflammatory Emo and anti-osteoporotic sCT. The current study indicates that this co-delivery system based on the thermosensitive PLGA–PEG–PLGA hydrogel is a simple and effective strategy with potential to address the urgent clinical need for prosthesis aseptic loosening prevention. However, the lack of independent and in-depth mechanism studies at the cellular level for sCT and Emo is a major limitation of this work.

Author contributions

Yang Wang: conceptualization, methodology, resources, investigation, data curation, formal analysis, visualization, and writing – original draft; Xin Wang: investigation and writing – review &

editing; Hongjie Zhang: investigation and writing – review & editing; Yaoben Wang: investigation and writing – review & editing; Hancheng Wang: investigation and writing – review & editing; Zhiyong Chen: investigation and writing – review & editing; Jiandong Ding: writing – review & editing; Xiaochun Peng: funding acquisition, investigation, supervision, and writing – review & editing; Lin Yu: funding acquisition, supervision, writing – original draft, and writing – review & editing.

Conflicts of interest

The authors declare no conflict of interest.

Data availability

The data supporting this article are included as part of the supplementary information (SI) and are also available from the corresponding author upon reasonable request.

Supplementary information is available. The size and distribution of copolymer micelles in water; optical images of the two-step method of loading of Emo in copolymer solution; optical images of the desolvation method of preparation of sCT/BSA NPs; the surface charge density calculation of sCT/BSA NPs; the secondary structure analysis of free sCT and sCT/BSA NPs; AFM images of BSA NPs, sCT/BSA NPs, free BSA and free sCT; HPLC measurement methods for sCT and Emo; histological section images of the air pouch membrane and bone-implanted pouch "sandwich"-like tissues. See DOI: https://doi.org/10.1039/d6bm00096g.

Acknowledgements

This work was supported by the National Natural Science Foundation of China (grant no. 22475052 and 82472461), the Natural Science Foundation of Shanghai (grant no. 23ZR1406800) and open research fund of Shanghai Key Laboratory of Gene Editing and Cell Therapy for Rare Diseases (grant no. gect-2025-Z15).

References

1 J. G. Betts, K. A. Young, J. A. Wise, E. Johnson, B. Poe, D. H. Kruse, O. Korol, J. E. Johnson, M. Womble and P. DeSaix, *Anatomy and Physiology*, OpenStax, Houston, 2nd edn, 2022.
2 M. F. Kong, V. Nayyar, R. Jogia, R. Berrington and S. Jackson, *Lancet*, 2008, **372**, 1854.
3 X. You, L. Q. Wu, L. L. Fu, Q. Q. Wu and B. R. Qi, *Eur. Cells Mater.*, 2025, **50**, 109–123.
4 I. D. Learmonth, C. Young and C. Rorabeck, *Lancet*, 2007, **370**, 1508–1519.
5 A. J. Carr, O. Robertsson, S. Graves, A. J. Price, N. K. Arden, A. Judge and D. J. Beard, *Lancet*, 2012, **379**, 1331–1340.
6 P. Sadoghi, M. Liebensteiner, M. Agreiter, A. Leithner, N. Böhler and G. Labek, *J. Arthroplasty*, 2013, **28**, 1329–1332.
7 Z. T. Deng, Z. H. Wang, J. W. Jin, Y. Wang, N. R. Bao, Q. Gao and J. N. Zhao, *Acta Biomater.*, 2017, **49**, 541–554.
8 X. Feng, J. M. Gu and Y. X. Zhou, *Am. J. Transl. Res.*, 2022, **14**, 7080–7089.
9 P. Drees, A. Eckardt, R. E. Gay, S. Gay and L. C. Huber, *Nat. Clin. Pract. Rheumatol.*, 2007, **3**, 165–171.
10 N. A. Hodges, E. M. Sussman and J. P. Stegemann, *Biomaterials*, 2021, **278**, 121127.
11 J. Gallo, S. B. Goodman, Y. T. Konttinen, M. A. Wimmer and M. Holinka, *Acta Biomater.*, 2013, **9**, 8046–8058.
12 J. Pajarinen, T. H. Lin, T. Sato, Z. Yao and S. B. Goodman, *J. Mater. Chem. B*, 2014, **2**, 7094–7108.
13 M. Couto, D. P. Vasconcelos, D. M. Sousa, B. Sousa, F. Conceiçao, E. Neto, M. Lamghari and C. J. Alves, *Front. Mater.*, 2020, **7**, 274.
14 S. Noordin and B. Masri, *Can. J. Surg.*, 2012, **55**, 408–417.
15 L. Zhang, E. Haddouti, K. Welle, C. Burger, D. C. Wirtz, F. A. Schildberg and K. Kabir, *Front. Cell Dev. Biol.*, 2020, **8**, 352.
16 Y. Xie, Y. J. Peng, G. T. Fu, J. W. Jin, S. Wang, M. Y. Li, Q. J. Zheng, F. J. Lyu, Z. T. Deng and Y. C. Ma, *Front. Cell. Infect. Microbiol.*, 2023, **13**, 1275086.
17 H. L. Sun, Y. D. Chen, X. Q. Sang, Q. X. Liu, H. R. Yu, S. J. Hu, Y. J. Mao and L. Zhang, *Regener. Biomater.*, 2025, **12**, rbaf006.
18 T. X. Geng, S. X. Sun, H. C. Yu, H. H. Guo, M. X. Zheng, S. Zhang, X. Chen and Q. H. Jin, *Braz. J. Med. Biol. Res.*, 2018, **51**, e7414.
19 K. C. Zhu, C. Yang, H. Y. Dai, J. H. Li, W. Liu, Y. Luo, X. L. Zhang and Q. Wang, *Int. Immunopharmacol.*, 2019, **76**, 105865.
20 T. L. Ma, J. X. Chen, Z. R. Ke, P. Zhu, Y. H. Hu and J. Xie, *Front. Bioeng. Biotechnol.*, 2022, **10**, 925841.
21 Z. F. Sun, J. N. Kang, S. Y. Yang, Y. Zhang, N. N. Huang, X. D. Zhang, G. Q. Du, J. H. Jiang and B. Ning, *Int. Immunopharmacol.*, 2023, **122**, 110561.
22 J. N. Xu, C. H. Zhang and J. B. Luo, *ACS Appl. Polym. Mater.*, 2022, **4**, 7487–7497.
23 Y. N. Li, P. P. Tian, H. Cao, Y. Wang, X. Zhao, S. Han and C. C. Wang, *Tribol. Int.*, 2024, **192**, 109229.
24 Y. Deng, K. Phillips, Z. P. Feng, P. N. Smith and R. W. Li, *J. Orthop. Surg. Res.*, 2024, **19**, 94.
25 W. He, N. Kapate, C. W. Shields and S. Mitragotri, *Adv. Drug Delivery Rev.*, 2020, **165–166**, 15–40.
26 X. F. Liu, J. S. Wu, R. M. Tian, S. Y. Su, S. A. Deng and X. L. Meng, *Biomed. Pharmacother.*, 2020, **129**, 110433.
27 C. M. Battistoni, J. M. Briones, D. K. Brubaker, A. Panitch and J. C. Liu, *Biomater. Sci.*, 2025, **13**, 3252–3263.
28 W. Deng, T. S. Wang, L. Li, X. Y. Xiao, Y. Y. Xu, Q. J. Li, Q. S. Zhou, Y. Yin, H. S. Yang, K. Gong, Y. Zhou and Y. B. Wang, *Regener. Biomater.*, 2025, **12**, rbaf048.
29 Y. H. Wang, W. Smith, D. J. Hao, B. R. He and L. B. Kong, *Int. Immunopharmacol.*, 2019, **70**, 459–466.

30 J. He, P. H. Yin and K. Xu, *Drug Des., Dev. Ther.*, 2020, **14**, 907–919.
31 T. Zhu, W. Zhang, S. J. Feng and H. P. Yu, *Int. Immunopharmacol.*, 2016, **34**, 16–24.
32 X. X. Dong, J. Fu, X. B. Yin, S. L. Cao, X. C. Li, L. F. Lin, Huyiligeqi and J. Ni, *Phytother. Res.*, 2016, **30**, 1207–1218.
33 S. Iwanowycz, J. F. Wang, D. Altomare, Y. Hui and D. P. Fan, *J. Biol. Chem.*, 2016, **291**, 11491–11503.
34 Y. P. Liu, X. B. Chen, S. Y. Li, Q. Guo, J. Xie, L. Yu, X. Y. Xu, C. M. Ding, J. S. Li and J. D. Ding, *ACS Appl. Mater. Interfaces*, 2017, **9**, 23428–23440.
35 S. Sladek, C. Kearney, D. Crean, P. A. J. Brama, L. Tajber, K. Fawcett, M. C. Labberte, B. Leggett and D. J. Brayden, *Drug Delivery Transl. Res.*, 2018, **8**, 1421–1435.
36 M. H. Liang, L. Zhou, J. Li, B. Liang, L. Y. Zhou, F. F. Xue, L. B. Jiang and W. Hong, *Regener. Biomater.*, 2025, **12**, rbaf028.
37 P. Yu, Y. P. Liu, J. Xie and J. S. Li, *J. Controlled Release*, 2021, **338**, 486–504.
38 P. Peichl, R. Marteau, A. Griesmacher, W. Kumpan, R. Schedl, E. Prosquil, P. Fasol and H. Bröll, *J. Bone Miner. Metab.*, 2005, **23**, 243–252.
39 I. O. Arnala, *Scand. J. Surg.*, 2012, **101**, 249–254.
40 H. Cai, A. N. Chen, Y. Y. You, J. X. Qu, V. Scheper, J. Tang and H. Z. Zhang, *Biomater. Sci.*, 2025, **13**, 5837–5850.
41 D. P. Wang, J. M. Yang, C. Liu, W. Lin, S. L. Lei, Y. X. Chen, P. Y. Cheng, Y. L. Huang, S. L. Gu, H. S. Li, Y. W. Lin, H. Z. Guo, G. Y. Mo, B. Mai, Z. Zhang, Q. T. Li, Y. X. Li, X. D. Cao and S. C. Zhang, *Composites, Part B*, 2025, **295**, 112195.
42 P. Yu, Y. P. Liu, R. T. Jin, P. Zhang, C. M. Ding, X. L. Jiang, J. Q. Xing, B. Bi, J. Xie and J. S. Li, *ACS Biomater. Sci. Eng.*, 2020, **6**, 4077–4086.
43 Y. C. Chen, S. F. Gad, D. Chobisa, Y. Z. Li and Y. Yeo, *J. Controlled Release*, 2021, **330**, 438–460.
44 X. Chen, C. Xu, T. X. Geng, Y. Geng, Z. H. Li, Y. Q. Li, P. Wu, N. N. Lei, X. J. Zhuang and S. J. Zhao, *ACS Appl. Mater. Interfaces*, 2024, **16**, 5368–5381.
45 X. L. Ma, Z. Wang, M. Alip, Q. Mao, C. Zhao, H. Y. Zhang, G. H. Yao, L. Y. Sun and L. Jiang, *Biomater. Sci.*, 2026, **14**, 871–884.
46 X. H. Wu, X. Wang, X. B. Chen, X. W. Yang, Q. Ma, G. H. Xu, L. Yu and J. D. Ding, *Bioact. Mater.*, 2021, **6**, 4717–4728.
47 Y. B. Wang, X. W. Yang, X. B. Chen, X. Wang, Y. Wang, H. C. Wang, Z. Y. Chen, D. L. G. Cao, L. Yu and J. D. Ding, *Adv. Funct. Mater.*, 2022, **32**, 2206554.
48 X. B. Chen, H. C. Wang, J. Y. Shi, Z. Y. Chen, Y. B. Wang, S. Y. Gu, Y. Fu, J. L. Huang, J. D. Ding and L. Yu, *Biomaterials*, 2023, **298**, 122139.
49 J. Pan, H. Z. Tian, S. M. Xu, L. W. Zhang, J. D. Ding, H. J. Wang, L. Yu, W. Fu and X. Liu, *Composites, Part B*, 2024, **271**, 111162.
50 H. C. Wang, Z. Y. Chen, S. Y. Gu, Y. B. Wang, Y. Wang, C. Y. Gao, J. Y. Shi, J. D. Ding, Q. H. Wang and L. Yu, *Theranostics*, 2026, **16**, 1833–1854.
51 Z. L. Wang, S. Y. Qiu, Y. Q. Sun, X. J. Du, C. F. Xu, Z. Y. Cao and Z. D. Lu, *Biomater. Sci.*, 2025, **13**, 3016–3029.
52 Z. Y. Guo, Y. Bai, Z. Z. Zhang, H. Mei, J. Li, Y. J. Pu, N. Zhao, W. X. Gao, F. Wu, B. He and J. Xie, *J. Mater. Chem. B*, 2021, **9**, 3874–3884.
53 Y. B. Wang, X. B. Chen, Z. Y. Chen, X. Wang, H. C. Wang, H. J. Zhai, J. D. Ding and L. Yu, *Bioact. Mater.*, 2024, **39**, 336–353.
54 X. Wang, Z. Y. Chen, Z. X. Wang, L. W. Zhang, J. D. Ding and L. Yu, *Acta Biomater.*, 2025, **205**, 346–361.
55 Y. Woo, M. Patel, H. Kim, J. K. Park, Y. J. Jung, S. S. Cha and B. Jeong, *ACS Appl. Mater. Interfaces*, 2022, **14**, 3773–3783.
56 Z. M. Li, W. G. Xu, J. Z. Yang, J. Wang, J. L. Wang, G. Zhu, D. Li, J. X. Ding and T. M. Sun, *Adv. Mater.*, 2022, **34**, 2200449.
57 Y. Moon, M. Patel, S. Um, H. J. Lee, S. Park, S. B. Park, S. S. Cha and B. Jeong, *J. Controlled Release*, 2022, **343**, 118–130.
58 J. Y. Shi, L. Yu and J. D. Ding, *Acta Biomater.*, 2021, **128**, 42–59.
59 J. Lee, J. Kim, J. Kim and S. C. Song, *Small*, 2025, **21**, 2502399.
60 J. Lee, J. Kim, K. W. Bong and S. C. Song, *Biomater. Sci.*, 2025, **13**, 6326–6349.
61 T. Vermonden, R. Censi and W. E. Hennink, *Chem. Rev.*, 2012, **112**, 2853–2888.
62 Y. P. Zhuang, X. W. Yang, Y. M. Li, Y. P. Chen, X. C. Peng, L. Yu and J. D. Ding, *ACS Appl. Mater. Interfaces*, 2019, **11**, 29604–29618.
63 J. J. Chang, Q. Y. Lin, N. Ong, J. H. M. Wong, V. Ow, B. Sim, C. Owh, R. Goh, J. Y. C. Lim and X. J. Loh, *Prog. Polym. Sci.*, 2025, **168**, 102004.
64 K. W. Lei, Y. Wang, X. C. Peng, L. Yu and J. D. Ding, *J. Polym. Sci.*, 2022, **60**, 2875–2888.
65 X. J. Loh, P. L. Chee and C. Owh, *Small Methods*, 2019, **3**, 1800313.
66 C. Weber, C. Coester, J. Kreuter and K. Langer, *Int. J. Pharm.*, 2000, **194**, 91–102.
67 F. Galisteo-González and J. A. Molina-Bolívar, *Colloids Surf., B*, 2014, **123**, 286–292.
68 S. Q. Cui, L. Yu and J. D. Ding, *Macromolecules*, 2019, **52**, 3697–3715.
69 H. C. Parkin, L. K. Shopperly, M. R. Perez, S. M. Willerth and I. Manners, *Biomater. Sci.*, 2024, **12**, 5283–5294.
70 R. Vijayaraghavan, M. Vidyavathi, R. V. S. Kumar, S. Loganathan and R. B. Valapa, *Biomater. Sci.*, 2025, **13**, 1286–1303.
71 V. M. Platon, A. M. Craciun, I. Rosca, N. Simionescu and L. Marin, *Biomater. Sci.*, 2026, **14**, 140–160.
72 C. C. Hou, S. H. Wang, Z. H. Li, Q. Huang, Y. Jiang, X. Zhou, R. Y. Ou, D. Y. Li and Y. S. Xu, *Regener. Biomater.*, 2025, **12**, rbaf051.
73 R. Y. Yin, Z. H. Guo, X. L. Lv, X. D. He, Z. W. Gao, W. Shen, X. Yi, P. Zhang, C. S. Xiao and X. S. Chen, *Biomacromolecules*, 2025, **26**, 7564–7575.
74 A. O. Elzoghby, W. M. Samy and N. A. Elgindy, *J. Controlled Release*, 2012, **157**, 168–182.

75 J. Y. Jun, H. N. Hoang, S. Y. R. Paik, H. S. Chun, B. C. Kang and S. Ko, *Food Chem.*, 2011, **127**, 1892–1898.
76 S. N. Tegopoulos, S. Ektirici, V. Harmandaris, A. Kyritsis, A. N. Rissanou and A. Papagiannopoulos, *Polymers*, 2025, **17**, 2125.
77 E. Apuzzo, M. Cathcarth, A. S. Picco, C. von Bilderling, O. Azzaroni, M. L. Agazzi and S. E. Herrera, *Biomacromolecules*, 2025, **26**, 1171–1183.
78 A. Allagui, H. Benaoum and O. Olendski, *Phys. A*, 2021, **582**, 126252.
79 K. T. Wu, X. B. Chen, S. Y. Gu, S. Q. Cui, X. W. Yang, L. Yu and J. D. Ding, *Macromolecules*, 2021, **54**, 7421–7433.
80 X. B. Chen, J. L. Zhang, K. T. Wu, X. H. Wu, J. Y. Tang, S. Q. Cui, D. L. Cao, R. L. Liu, C. Peng, L. Yu and J. D. Ding, *Small Methods*, 2020, **4**, 2000310.
81 W. Ren, S. Y. Yang and P. H. Wooley, *Scand. J. Rheumatol.*, 2004, **33**, 349–357.
82 P. H. Wooley, R. Morren, J. Andary, S. A. Sud, S. Y. Yang, L. Mayton, D. Markel, A. Sieving and S. Nasser, *Biomaterials*, 2002, **23**, 517–526.